

University of Groningen

## A Flip-Over Plasmonic Structure for Photoluminescence Enhancement of Encapsulated WS<sub>2</sub> Monolayers

Liang, Minpeng; Han, Chunrui; Zheliuk, Oleksandr; Chen, Qihong; Wan, Puhua; Peng, Xiaoli; Zhang, Le; Ye, Jianting

*Published in:*  
Advanced optical materials

*DOI:*  
[10.1002/adom.202100397](https://doi.org/10.1002/adom.202100397)

**IMPORTANT NOTE: You are advised to consult the publisher's version (publisher's PDF) if you wish to cite from it. Please check the document version below.**

*Document Version*  
Publisher's PDF, also known as Version of record

*Publication date:*  
2021

[Link to publication in University of Groningen/UMCG research database](#)

*Citation for published version (APA):*

Liang, M., Han, C., Zheliuk, O., Chen, Q., Wan, P., Peng, X., Zhang, L., & Ye, J. (2021). A Flip-Over Plasmonic Structure for Photoluminescence Enhancement of Encapsulated WS<sub>2</sub> Monolayers. *Advanced optical materials*, 9(16), [2100397]. <https://doi.org/10.1002/adom.202100397>

**Copyright**

Other than for strictly personal use, it is not permitted to download or to forward/distribute the text or part of it without the consent of the author(s) and/or copyright holder(s), unless the work is under an open content license (like Creative Commons).

The publication may also be distributed here under the terms of Article 25fa of the Dutch Copyright Act, indicated by the "Taverne" license. More information can be found on the University of Groningen website: <https://www.rug.nl/library/open-access/self-archiving-pure/taverne-amendment>.

**Take-down policy**

If you believe that this document breaches copyright please contact us providing details, and we will remove access to the work immediately and investigate your claim.

Downloaded from the University of Groningen/UMCG research database (Pure): <http://www.rug.nl/research/portal>. For technical reasons the number of authors shown on this cover page is limited to 10 maximum.

# A Flip-Over Plasmonic Structure for Photoluminescence Enhancement of Encapsulated WS<sub>2</sub> Monolayers

Minpeng Liang, Chunrui Han, Oleksandr Zheliuk, Qihong Chen, Puhua Wan, Xiaoli Peng, Le Zhang, and Jianting Ye\*

Transition metal dichalcogenide (TMD) monolayers, with their direct band gaps, have attracted wide attention from the fields of photonics and optoelectronics. However, monolayer semiconducting TMDs generally suffer from low excitation absorption and emission efficiency, limiting their further applications. Here a flip-over plasmonic structure comprised of silver nano-disk arrays supporting a WS<sub>2</sub> monolayer sandwiched by hexagonal boron nitride (*h*-BN) layers is demonstrated. The flip-over configuration optimizes the optical process with a free excitation/emission path from the top and a strong plasmonic interaction from the bottom. As a result, the photoluminescence from the TMD monolayers can be greatly enhanced more than tenfold by optimizing the metasurface, which can be further improved nearly tenfold by optimizing the thickness of bottom *h*-BN. This study shows the advantages of using the flip-over structure, where the plasmonic interaction between the metasurface and TMDs can be tuned by introducing optimized plasmonic arrays and *h*-BN layers with suitable thickness. This hybrid device configuration paves a reliable platform to study the light–matter interaction, achieving highly efficient plasmonic TMD devices.

## 1. Introduction

Plasmonic metasurfaces made of noble metals can confine and enhance electromagnetic (EM) fields that enables a wide range of applications in optical spectroscopy.<sup>[1–5]</sup> Recently, integrating the plasmonic structures with active optical media is attracting growing interest<sup>[2,6,7]</sup> because the metasurface can effectively enhance the optical processes in the active media. One of these hybrid structures is composed by integrating 2D transition metal dichalcogenide (TMD) monolayers with plasmonic structures, where radiation enhancements were observed in Raman scattering,<sup>[8–10]</sup> light absorption,<sup>[11]</sup> photoluminescence,<sup>[9,10,12,13]</sup> and second harmonic generation.<sup>[14,15]</sup>

To achieve a strong interaction between TMDs and the plasmonic structure, customizing the plasmonic metasurface and optimizing the excitonic process in TMDs

are two fundamental approaches.<sup>[13,16]</sup> Physically, both optimizations are characterized by the length scales involved in these two processes. For the plasmonic process, the typical length scale is the dimension of the evanescent field which can be of the order of half the wavelength of light involved.<sup>[17]</sup> On the other hand, a strong excitonic process can be found in TMD monolayers, where direct band gaps are present. The excitons are affected by the uneven potential from its direct environment, for example, the substrate, with a characteristic length scale of screening length. This is in the order of a few nanometers by considering the doping effect from the intrinsic defect density of  $\approx 10^{12} - 10^{13} \text{ cm}^{-2}$  in TMDs grown by chemical vapor deposition (CVD).<sup>[18]</sup> Furthermore, attaching TMDs to the close vicinity of a metasurface can also introduce additional length scale due to the metastructure itself. Since the thickness of nano-disk is tens of nanometers, the TMDs on the metasurfaces can be influenced by the stress caused by the corrugations having a length scale similar as the nanostructures at the bottom of the TMDs. Taking aforementioned length scales into consideration, optimizing the PL in TMDs becomes a multi-factor problem, which is yet to be studied fully by manipulating all relevant length scales.

To simplify this multi-factor tuning, it is necessary to pin down a few parameters that are known to be optimized. For the plasmonic structures, a silver nanostructure is widely used because of the low damping rate in the visible and near-infrared range.<sup>[7,19,20]</sup> Apart from different array geometries, nano-disks


M. Liang, Dr. O. Zheliuk, P. Wan, X. Peng, Dr. L. Zhang, Prof. J. Ye  
Device Physics of Complex Materials  
Zernike Institute for Advanced Materials  
University of Groningen  
Nijenborgh 4, Groningen 9747 AG, The Netherlands  
E-mail: j.ye@rug.nl

Prof. C. Han  
Institute of Microelectronics  
Chinese Academy of Sciences  
Beijing 100029, China

Prof. C. Han, Prof. Q. Chen  
University of Chinese Academy of Sciences  
Beijing 100049, China

Prof. Q. Chen  
Beijing National Laboratory for Condensed Matter Physics  
Institute of Physics, Chinese Academy of Sciences  
Beijing 100190, China

Dr. L. Zhang  
Shenzhen Key Laboratory of Laser Engineering  
College of Physics and Optoelectronic Engineering  
Shenzhen University  
Shenzhen 518060, China

 The ORCID identification number(s) for the author(s) of this article can be found under <https://doi.org/10.1002/adom.202100397>.

© 2021 The Authors. Advanced Optical Materials published by Wiley-VCH GmbH. This is an open access article under the terms of the Creative Commons Attribution License, which permits use, distribution and reproduction in any medium, provided the original work is properly cited.

DOI: 10.1002/adom.202100397

with a thickness of tens of nanometers are widely used because they are not only easy to fabricate but also show strong plasmonic resonance.<sup>[21]</sup> For the optical media, the CVD-grown TMD monolayers are the preferable choice compared with the cleaved ones. Because of the much larger area, the CVD monolayer can interact with a larger metastructure array, where plasmonic response is better defined.<sup>[22]</sup> After fixing the points above, researchers have tried to fabricate plasmonic structures directly on top of the CVD-grown TMD flakes.<sup>[12,13,21,23]</sup> Although the structures are easy to fabricate, depositing the plasmonic structure on top of the optical media can partially block the free optical path for both excitation and emission, reducing the PL efficiency of TMD monolayers. In addition, making metastructures directly on top of TMDs inevitably introduces surface contamination, which causes a degradation in the optical performance. A refined performance in PL is expected if the metasurface can be placed beneath the TMDs because it can open up a free path for both exciting and emitting radiation. Moreover, it is well known that the optical performance of TMD monolayers can be enhanced significantly by encapsulating TMDs between two *h*-BN flakes. Without a full encapsulation, the PL from the TMDs can be easily influenced by the change of doping, which can be caused even by vacuuming the device.<sup>[24]</sup> Similar concern also goes to the direct preparation of nano-structures on top of TMDs. As discussed above, the direct micro-fabrication on TMDs without encapsulation can induce surface contamination, hence also affect the excitonic process of TMD monolayers. These aforementioned sensitive dependencies preclude a reliable analysis that is intended to disentangle the multiple enhancement factors contributed by the hybrid structure. Therefore, a full encapsulated monolayer becomes a prerequisite to reliably analyze the enhancement effect in the TMD/nano-disk devices with a flip-over configuration.

After fixing the optimized ingredients, the tunable length scale parameters are then narrowed down to 1) the layout of the metal disk array such as the pitch size ( $P$ ) and diameter ( $D$ ), which is responsible for the wavelength and strength of the plasmonic resonance. 2) The thickness of the bottom *h*-BN of the sandwiched heterostructure, which determines the excitonic process of TMDs and the interactive strength between plasmonic structures and TMDs. Although a single layer of *h*-BN can already isolate the doping effect from the substrate effectively, it requires a much thicker *h*-BN to smooth out the corrugation caused by the nano-disks that is tens of nanometer in height if the metamaterials are buried below the heterostructure in the flip-over configuration.

## 2. Results and Discussion

By incorporating the considerations introduced above, as shown schematically in **Figure 1a**, we fabricated a hybrid structure composed of a sandwiched heterostructure: *h*-BN/WS<sub>2</sub>/*h*-BN, which was then laminated onto silver (Ag) disk arrays with different pitches and diameters. The WS<sub>2</sub> monolayers used in this study were prepared by CVD. For better consistency, large-area metasurface and CVD-grown WS<sub>2</sub> monolayers with uniform PL were chosen. The WS<sub>2</sub> monolayers were grown in the same

batch, which ensured the consistency in the crystal quality. We chose a thick top *h*-BN (from 80 to 100 nm) to fully encapsulate the TMD monolayer. The dielectric property of thick *h*-BNs is close to the bulk, thus the thickness differences of the top *h*-BNs has no appreciable effect on the optical performance.

For the metasurface, we fabricate nano-disks with fixed diameter  $D = 180$  nm, which are composed of 50 nm Ag and  $\approx 2$  nm Al<sub>2</sub>O<sub>3</sub>. The Ag and Al<sub>2</sub>O<sub>3</sub> overlayers are deposited by e-beam evaporation and atomic layer deposition (ALD), respectively. The highly conformal covering of Al<sub>2</sub>O<sub>3</sub> grown by ALD can effectively prevent the Ag nano-disk from oxidation and the direct contact between the metal and TMD, which quenches the excitons. The layout of the metasurface is shown in the SEM image, where uniform Ag nano-disks form a square lattice (**Figure 1b**). As shown in **Figure 1c**, a clear color change can be directly observed in the optical reflections from the arrays with pitch sizes from  $P = 220$  to 380 nm. The plasmonic effect can be seen as a change in the color tone toward longer wavelength with the increase of pitch size  $P$ . For a fixed array size, larger pitch size also means larger surface uncovered by the metal disks. Consistently, we observed that the intensity of reflection decreases because the fraction of area covered by the metal disk reduces with the increase of pitch size from 220 to 380 nm. These direct observations in the variations of reflection from different metasurfaces was further verified by the reflection spectra shown in **Figure S1**, Supporting Information.

On the other hand, for the active optical media in this hybrid device, we choose large-area WS<sub>2</sub> monolayer grown by CVD (left top inset in **Figure 1d**). The PL from the as-grown flake shows typical monolayer spectrum centered at 632.7 nm (the right inset in **Figure 1d**). The PL intensity is distributed uniformly across the whole flake as-shown in the PL imaging (left bottom panel, inset of **Figure 1d**). The uniformity of the PL from the CVD WS<sub>2</sub> is characterized by the brightness histogram. For a typical monolayer flake with an area of  $\approx 625 \mu\text{m}^2$  (left bottom inset of **Figure 1d**), the full width at half maximum of pixel brightness is 8.5 for a total intensity centered at 123 counts. This corresponds to less than 7% intensity variation, confirming the good uniformity of our monolayer WS<sub>2</sub> grown by CVD. To further check the quality of WS<sub>2</sub> monolayer, the Raman spectrum of WS<sub>2</sub> flake was taken, as shown in **Figure 1e**. The characteristic Raman features are consistent with those from the WS<sub>2</sub> monolayers, where the features at 350 and 416.5 cm<sup>-1</sup> correspond to the in-plane ( $E_{2g}^1$ ) and out-of-plane ( $A_{1g}$ ) modes, respectively. The difference between the two modes is 66.5 cm<sup>-1</sup>, which is consistent to the reported value (65.5 cm<sup>-1</sup>) for monolayer WS<sub>2</sub>.<sup>[25]</sup> Therefore, our characterizations confirm the high quality of both metasurface and WS<sub>2</sub> monolayer as the prerequisites for reliable analysis on the enhancement in the hybrid structures.

Before assembling the device, we characterized the optical properties of metamaterials. As shown in **Figure 1f**, we measured the optical absorption (1-transmission-reflection) for the metasurfaces shown in **Figure 1c**. In the spectral range between 550–680 nm, the absorption spectra is characterized by strong dipole resonance peaks, which shows a clear blue-shift with the decrease of  $P$  from 380 to 260 nm. In the wavelength range lower than the dipole resonance peak, we observed several broad resonance peaks, which can be attributed to the

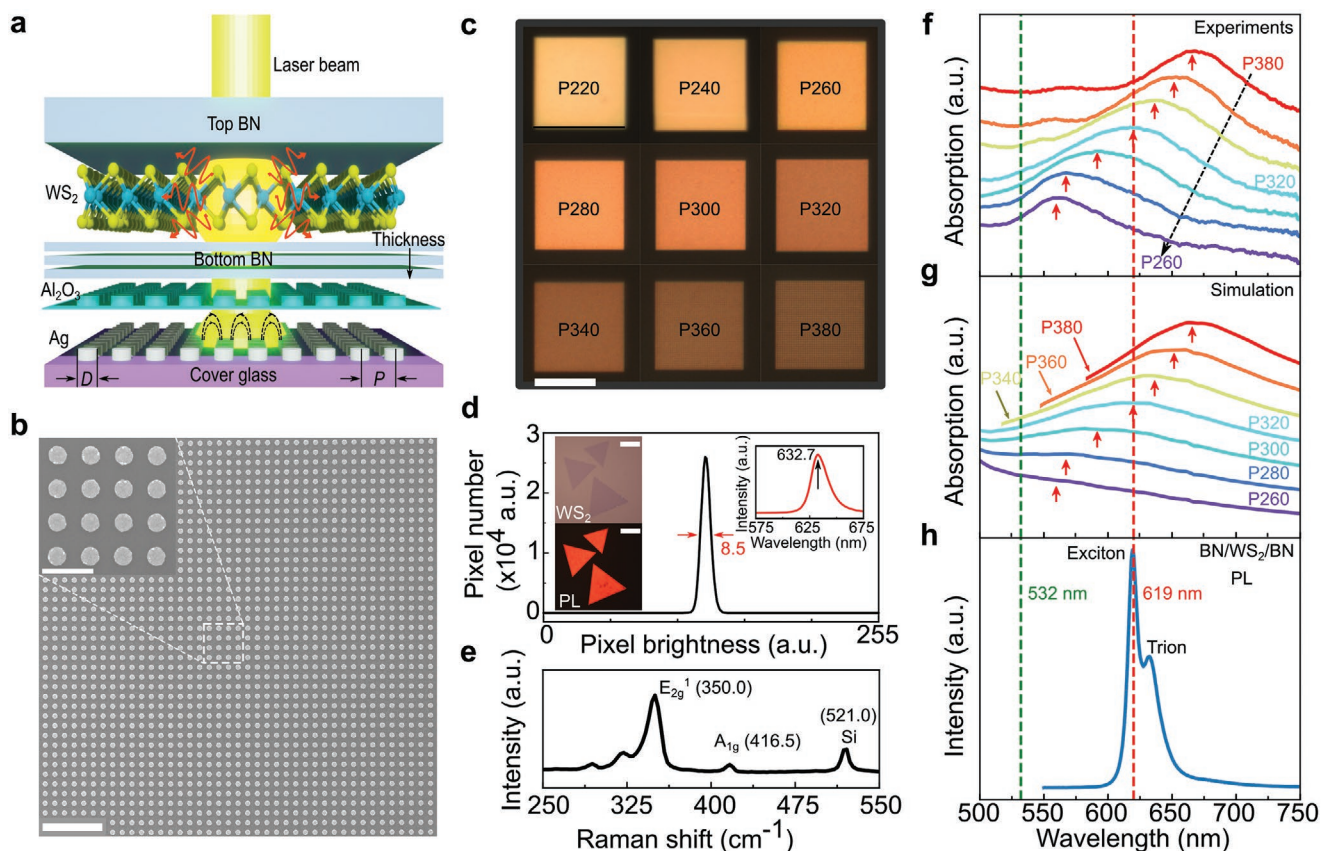


**Figure 1.** Device structure and the property of each component. a) A schematic illustration of the device structure. b) The SEM images of nano-disk arrays with diameter  $D = 180$  nm and pitch size  $P = 320$  nm. The scale bars in panel (b) and its insert are  $2 \mu\text{m}$  and  $500$  nm, respectively. c) Optical images of the silver nano-disk arrays, the scale bar is  $10 \mu\text{m}$ . The  $D$  is  $180$  nm for all arrays and the  $P$  values are  $220$ ,  $240$ ,  $260$ ,  $280$ ,  $300$ ,  $320$ ,  $340$ ,  $360$ , and  $380$  nm, respectively. d) Brightness histogram of PL image for a measured area of  $625 \mu\text{m}^2$ . The optical and PL images of the measured TMD monolayers are shown in the left insets of panel (d), both scale bars are  $20 \mu\text{m}$ . The right inset in panel (d) shows the PL spectrum of a as-grown  $\text{WS}_2$  monolayer on  $\text{SiO}_2$ . e) Raman spectrum of a as-grown  $\text{WS}_2$  monolayer. f) Absorption measurements and g) the FDTD simulation of arrays with pitch sizes from  $260$  to  $380$  nm. h) PL spectrum of  $h$ -BN encapsulated  $\text{WS}_2$  measured at  $293$  K. The dashed green vertical line corresponds to the laser excitation wavelength ( $532$  nm). The red dashed line corresponds to the PL emission peak position ( $619$  nm) of  $h$ -BN encapsulated  $\text{WS}_2$ .

high-order plasmon resonance modes.<sup>[26]</sup> The blue-shift in the optical absorbance can be reproduced with the simulation by the finite difference time-domain (FDTD) calculation (Figure 1g). The trend of evolution of the dipole modes shows a good agreement with the experimental results. The mismatch in the overall shape and small shift in the position of peak features between FDTD calculation and experiment could be due to the imperfection in silver nano-disk arrays and the use of high numerical aperture objective ( $100\times$ ,  $\text{NA} = 0.9$ ) in the measurements, which includes the response from different angles.<sup>[13]</sup>

As shown in Figure 1h, the PL spectrum of the  $h$ -BN sandwiched  $\text{WS}_2$  monolayer (shaded in gray) falls into the spectral range of all plasmonic resonances shown in Figure 1f. Especially, when  $P = 320$  nm, the peak position of dipole resonance directly coincides with the maximum of the PL spectral profile ( $619$  nm) of  $\text{WS}_2$ , as indicated by the dashed red line. The spectral matching of excitation and emission with the plasmonic response plays a critical role in the PL enhancement. The matching of the excitation (the dashed green line at  $532$  nm) and the cavity response of the metamaterial can

enhance the excitation rate. On the other hand, the match between plasmon resonance and emission peak will improve the rate of radiative decay and the quantum efficiency by the Purcell effect.<sup>[27–30]</sup> Therefore, the optimized enhancement in PL should be achieved by the combined optimization in excitation and emission, namely, optimizing plasmon resonance to match the excitation and the emission. In present case, the excitation and emission wavelength overlap simultaneously with the main plasmonic resonance mode when  $P$  changes from  $260$  to  $320$  nm, implying that PL enhancement from TMD is optimized for pitch size in this range.

Figure 2a,b shows the optical image and fluorescence image of device 1 ( $D_1$ ). A large  $\text{WS}_2$  monolayer was encapsulated by  $h$ -BN, the thicknesses of the bottom (enclosed by the red dashed line) and top (green dashed line)  $h$ -BN are  $25.5$  and  $79$  nm, respectively. The pitch sizes of the arrays ( $4 \times 4 \mu\text{m}^2$ ) range from  $260$  to  $380$  nm. The different PL intensities from different arrays can be directly observed in the fluorescent image (Figure 2b). And the PL spectra of  $D_1$  with pitch sizes from  $260$  to  $380$  nm are presented in the left panel of Figure 2c. Two main peaks observed at  $620$  and  $632$  nm are

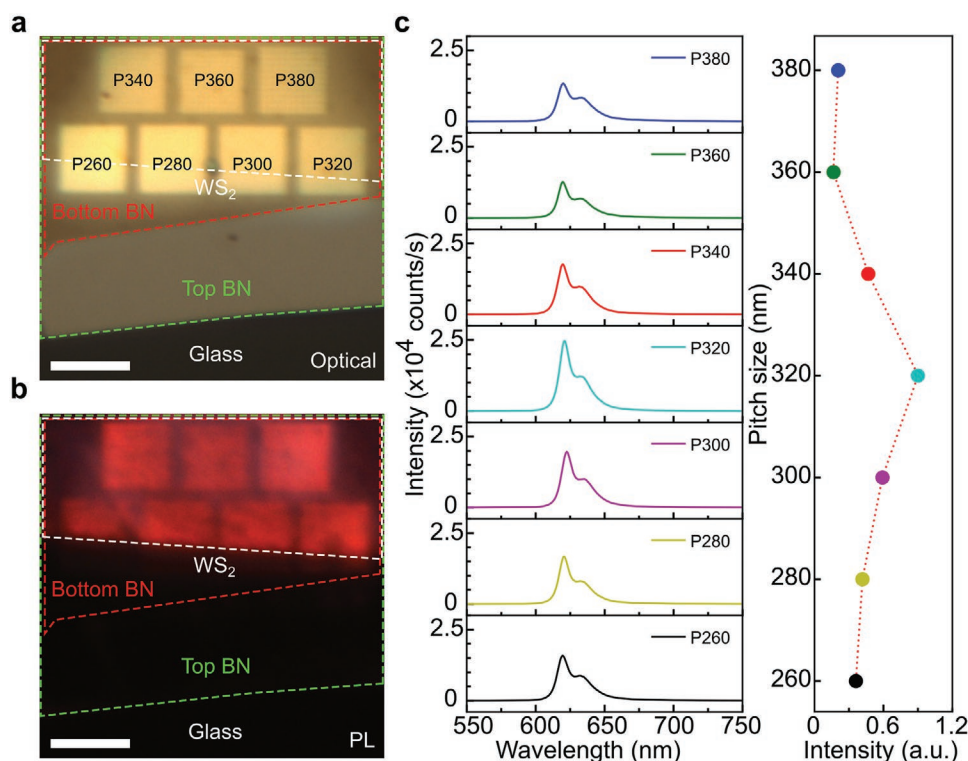


**Figure 2.** Device 1 ( $D_1$ ): Optimizing the pitch size of the metal disk array to enhance the PL. a) Optical image of  $D_1$ , the pitch sizes of the arrays are from 260 to 380 nm. The area enclosed by the white-dashed lines belongs to the monolayer  $WS_2$ , the green lines indicate the top  $h$ -BN and the red lines indicate the bottom  $h$ -BN. The value after “P” denotes the pitch size in nm. b) Fluorescence image of  $D_1$ , the excitation is at 462 nm. c) The left panel shows the PL spectra from the device with pitch sizes from 260 to 380 nm excited at 532 nm. And the right panel shows the main peak intensity of the spectra from the left panel. The scale bars in panel (a) and (b) are 5  $\mu$ m.

originated from the excitons and trions, respectively. For the array  $P = 260$  nm, the peak intensity is around 16 000 counts per second. The PL intensity increases to its maximum, more than 25 000 counts per second, when  $P$  increases to 320 nm, which is consistent with our evaluation made in Figure 1. After reaching the maximum, the PL intensity decreases to around 12 000 counts per second with the further increase of the pitch size to 380 nm. This maximizing scenario is plotted in the right panel of Figure 2c. Clear enhancement can be reproducibly achieved by including the metasurface of different pitch sizes. In comparison, the PL directly from the sandwiched monolayer appears much darker. The enhancement can be easily over tenfold compared with the area without the metasurface, where is enclosed by the dashed white lines shown in Figure 2b.

For the plasmonic metasurface, the pitch size can be optimized by the aforementioned steps. On the other hand, the excitonic process in TMD monolayer can be improved by adding a layer of bottom  $h$ -BN, which changes the dielectric environment of the TMD monolayer. This full encapsulation also affects the length scale related to the screening of the polar surface of  $SiO_2$  and improving the substrate flatness. Figure 3a,b shows the optical image and the corresponding fluorescent image of the device 2 ( $D_2$ ), which is designed to explore the effect of PL enhancement contributed by the bottom  $h$ -BN. As illustrated schematically in Figure 1a, the device configuration is affected by the relative position of the metasurface, the bottom  $h$ -BN, and the  $WS_2$ . In the device shown in

Figure 3a, the bottom  $h$ -BN layer has two regions marked as  $B$ -BN<sub>1</sub> and  $B$ -BN<sub>2</sub> with thicknesses of 6 and 12 nm, respectively. At locations marked as  $P_1$  to  $P_6$ , the PL spectra were measured on a single domain of a optically uniform  $WS_2$  monolayer. At each position, we measure the PL (as shown in Figure 3c) for the device configuration illustrated in the inset of Figure 3b at room temperature. Without having both the plasmonic array and the bottom  $h$ -BN, position  $P_1$  shows the lowest PL intensity corresponding to the top  $h$ -BN covers  $WS_2$  monolayer on  $SiO_2$  substrate. With bottom  $h$ -BN, the  $P_2$  location shows a stronger PL than  $P_1$ , indicating that having  $h$ -BN as the substrate can effectively isolate the doping effect from the polar substrate of  $SiO_2$ . Moreover, the  $h$ -BN also provides a better dielectric environment and a flatter substrate that also enhance the PL of  $WS_2$ .<sup>[31]</sup> For  $P_3$ , the  $WS_2$  monolayer is directly in contact with the metasurface. Interacting with the plasmonic modes can significantly enhance the PL even in the metastructure array without an optimized pitch size. Therefore, the PL at  $P_3$  is stronger compared with the environment without the help of metasurface ( $P_2$  and  $P_1$ ), which is consistent with the result shown in Figure 2. The comparison between  $P_3$  and  $P_2$  also suggests the dominating role of plasmonic arrays compared with the contribution from bottom  $h$ -BN. With the enhancement contribution from both plasmonic structures and bottom  $h$ -BN, the  $P_4$ ,  $P_5$ , and  $P_6$  have similar levels of strong PL enhancement. As shown in Figure 3c, the PL enhancements from different positions, if compared with the  $P_1$  (without both bottom  $h$ -BN and

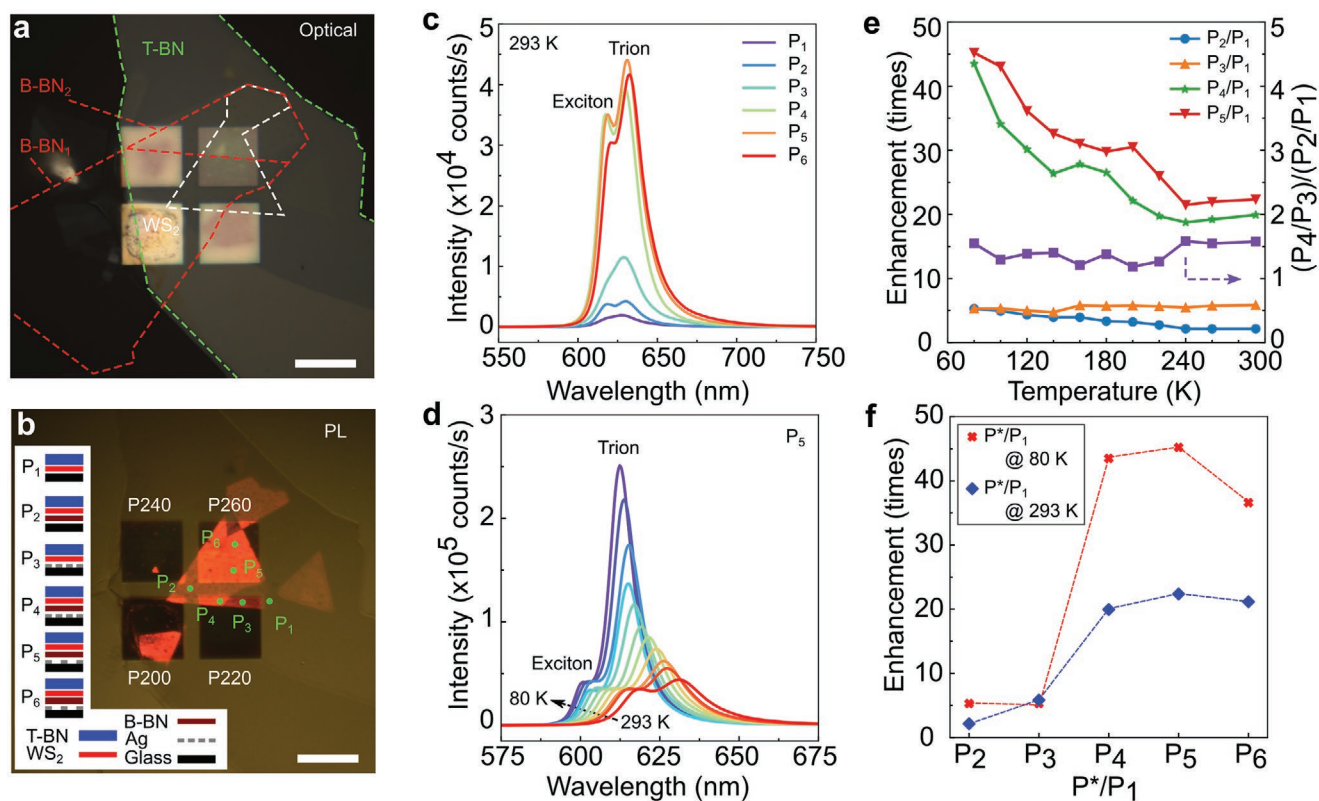


**Figure 3.** Device 2 ( $D_2$ ): PL enhancement contributed by bottom  $h$ -BN and plasmonic arrays. a) The optical image of  $D_2$ . The white area indicates the monolayer  $WS_2$ , the green area is the top  $h$ -BN (T-BN) and the red area is bottom  $h$ -BN (B-BN). B-BN<sub>1</sub> and B-BN<sub>2</sub> indicated the  $h$ -BN with thickness of 6 and 12 nm, respectively. b) The fluorescence image of (a). The red area shows the PL emission from the monolayer region. The PLs are measured at locations marked with green dots. And the vertical device structure at each dot is shown in the insert. c) PL spectra of  $P_1$ – $P_6$  at 293 K. d) Temperature dependence PL of  $P_5$  from 293 to 80 K. e) The temperature dependence of PL intensity compared to  $P_1$ . The data used here is the intensity maximum of each PL spectrum. f) PL enhancement of bottom  $h$ -BN and plasmonic arrays at 80 and 293 K.  $P_2/P_1$  measures the enhancement contribution of bottom  $h$ -BN.  $P_3/P_1$  measures the enhancement contribution of silver nano-disk arrays.  $P_4/P_1$  shows the enhancement from both bottom  $h$ -BN and plasmonic arrays.  $(P_4/P_3)/(P_2/P_1)$  shows the importance of bottom  $h$ -BN on the metastructure arrays compared with that measured on cover glass. Scale bars in panel (a) and (b) are 15  $\mu$ m.

plasmonic arrays), can be clearly divided into two groups. The PLs measured at  $P_2$  and  $P_3$  show moderate enhancement due to the single-factor contribution coming from either bottom  $h$ -BN or metasurface, respectively. Whereas, at  $P_4$  to  $P_6$ , the stronger PLs benefit from the dual-factor enhancement. The PL intensity of  $P_5$  is slightly stronger than  $P_4$  because, compared with  $P_4$  ( $P = 220$  nm), the  $P_5$  ( $P = 260$  nm) is closer to the optimized pitch size  $P = 320$  nm (Figure 2) of the metasurface.

The physical nature of having excitonic or plasmonic enhancement can be distinguished as a function of temperature. We measured the temperature dependence of PL to separate the enhancement contribution from the metasurface and bottom  $h$ -BN for different device configurations shown in Figure 3b. For a typical position  $P_5$ , where both enhancement factors are contributing, the peaks of both trion and exciton show blue-shift with the decrease of temperature. In addition, while the intensity of exciton almost remains constant, the intensity of trion increases significantly when temperature decreases. Namely, with the decrease of temperature, the excitation creates more exciton and trion. Meanwhile, it is also more efficient to bind the excitons with free carriers and form the trions due to the weaker thermal dissociation effect at lower temperature.<sup>[32]</sup>

As shown in Figure 3e, we measure other points for the temperature dependence of PL between 80 and 293 K. From the PL ratio measured between the points, we can disentangle the temperature dependence of enhancement factors. First of all, the enhancement ratio  $P_2/P_1$  isolates the effect of bottom  $h$ -BN, which increases with the decrease of temperature. Using the  $h$ -BN encapsulation, the excitonic process in  $WS_2$  monolayers can be well separated from the polar  $SiO_2$  substrate. As a result, the excitonic process is enhanced compared with monolayers on  $SiO_2$  substrate and becomes more efficient with the decrease of temperature. In contrast, the ratio  $P_3/P_1$  isolates the contribution from metasurface, which almost remains constant with the change of temperature. This suggests that the contribution from plasmonic enhancement is nearly temperature-independent. Consistently, the  $P_5/P_1$  and  $P_4/P_1$  show a continuous increase with the decrease of temperature due to the contribution from the bottom  $h$ -BN, which shows temperature dependence for the PL enhancement. The ratios between  $P_4/P_3$  and  $P_2/P_1$  (right y-axis of Figure 3e) show the effect of PL enhancement due to the bottom  $h$ -BN for the two cases of having the metasurface and the  $SiO_2$  as the bottom substrates, respectively. The  $(P_4/P_3)/(P_2/P_1)$  ratio is always above 1 from

80 to 293 K. Considering the interaction with the metasurface, the device at  $P_3$  should have a larger plasmonic enhancement compared with  $P_4$  (the  $WS_2$  at  $P_3$  is closer to the plasmonic arrays). This reverse dependence indicates that depositing the bottom  $h$ -BN on the metasurface plays a more important role than that on the cover glass, which could be attributed to the flatness differences of these two substrates. Since the substrate flatness is very important to the optical performance of 2D TMDs monolayers,<sup>[33]</sup> it is expected that the optical performance will be affected by the nano-disk array with a height 50 nm, which causes uneven substrate compared with the flat  $SiO_2$  substrate. Hence, the bottom  $h$ -BN can show a stronger effect to smooth out the substrate of the metasurface.

Sorted with the amount of enhancement, Figure 3f shows the PL enhancement measured at 80 K (red) and 293 K (blue) for the trion component measured from different positions. The comparison is normalized using the PL from  $P_1$  as the benchmark. At 293 K, the PL enhancement ratio of  $P_2$  (with contribution only from bottom  $h$ -BN) is only 2.5 times, which goes up to 5 times at 80 K. With the enhancement only from the plasmonic structure,  $P_3$  shows fivefold enhancement at 293 K, and the enhancement stays identical when temperature decreases to 80 K. The PL from  $P_4$ ,  $P_5$ , and  $P_6$  shows the strong enhancement already at 293 K, which nearly doubles at 80 K. This high ratio observed at  $P_4$ ,  $P_5$ , and  $P_6$  has taken the contributions from both plasmonic structures and bottom  $h$ -BN. The metasurface enhancement is nearly temperature-independent, which mounts up to  $\sim$ tenfold. On top of that, the bottom  $h$ -BN contributes the temperature-dependent part of the enhancement, which increases the total enhancement from  $\approx$ 22 to 45-fold ( $P_5$ ) when temperature decreases from 293 to 80 K.

Since the plasmonic enhancement effect comes from the evanescent field, it decays exponentially with the distance away from the surface of the metastructure array. Therefore, it is worthy of studying the enhancement of PL as a function of the thickness of the bottom  $h$ -BN. To systematically compare the thickness dependence, we refer the benchmark PL from a sandwiched  $WS_2$  with a bottom  $h$ -BN thickness equals to 52.5 nm, without the metasurface. As shown in Figure 4a, for the sample having metasurface but without bottom  $h$ -BN (i.e., bottom  $h$ -BN thickness is 0 nm), the PL intensity of  $WS_2$  is weaker compared with the positions with both array and bottom  $h$ -BN. Nevertheless, the PL is still stronger than the one only with bottom  $h$ -BN (52.5 nm). For samples on the metal arrays, the PL intensity increases first and then decreases, which appears different from our initial understanding that the plasmonic enhancement effect decays monotonically with the increase of separation, which increases with the increase of the thickness of bottom  $h$ -BN. The strongest PL intensity is achieved when the thickness of bottom  $h$ -BN is 45 nm, where 8.5- and 4.4-fold enhancements were obtained compared with that measured on the array but without bottom  $h$ -BN at 80 and 293 K, respectively. However, the enhancements become 13.1- and 15.6-fold at 80 and 293 K when compared to the configuration without array but with 52.5 nm bottom  $h$ -BN. There are two main factors that affect the PL enhancement: the plasmonic array structures (for the plasmonic enhancement) and the bottom  $h$ -BN (for the dielectric environment and substrate flatness). For a given plasmonic array, with the increase of thickness of bottom  $h$ -BN, the PL enhancement from plasmonic array decreases due to the diminishing coupling with the metasurface. However, thicker bottom  $h$ -BN can improve substrate flatness and the dielectric

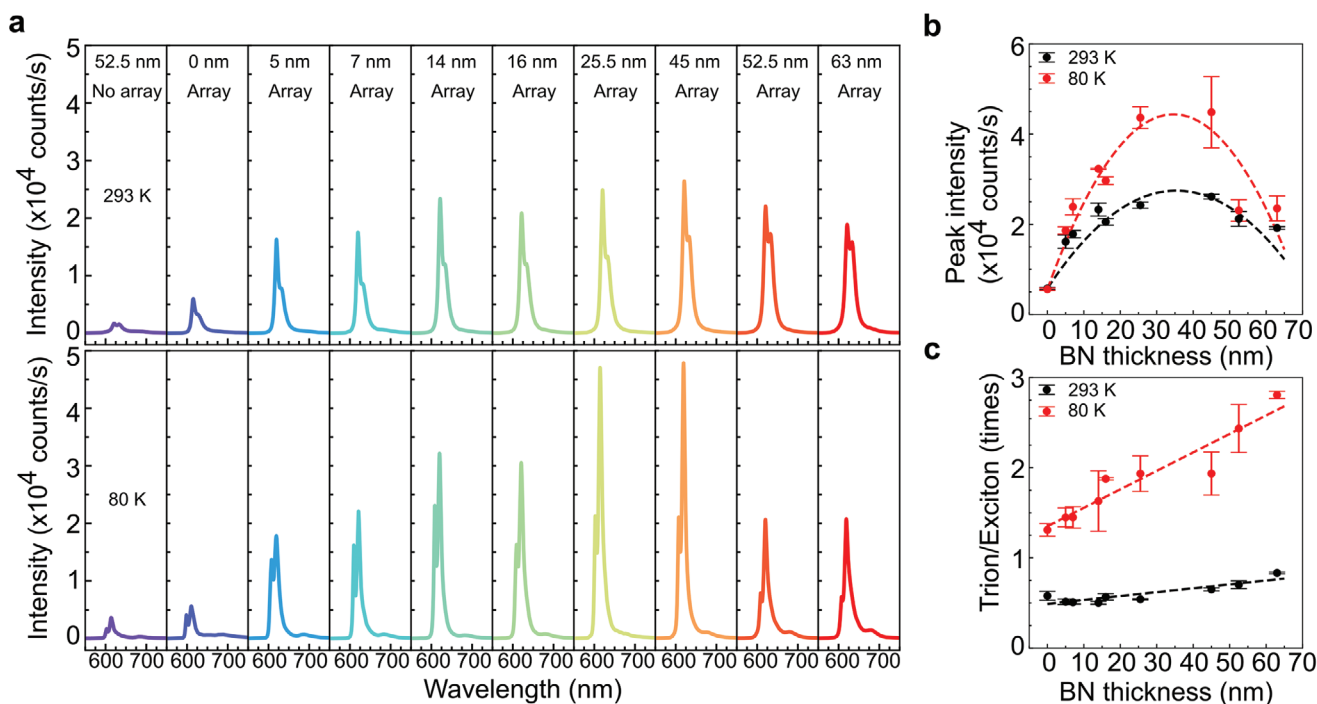


**Figure 4.** Device 3 ( $D_3$ ): The PL enhancement and trion/exciton ratio as a function of the bottom  $h$ -BN thickness a) PL spectra measured at 293 K (top panel) and 80 K (bottom panel). b) The PL peak intensity as a function of thickness of bottom  $h$ -BN at 293 and 80 K. c) The trion/exciton ratio as a function of the thickness of bottom  $h$ -BN at 293 and 80 K.

environment, which enhances the excitonic process, thus enhances the PL. When the thickness of bottom *h*-BN is less than 25.5 nm, the effect of the substrate flatness and dielectric environment outweighs the decay of plasmonic interaction. Therefore, the overall PL increases with the increase of bottom *h*-BN thickness. And the PL intensity reaches the maximum when the thickness of the bottom *h*-BN is between 25.5 and 45 nm. This corresponds to an optimized balancing of the two aforementioned contributions. When the bottom *h*-BN thickness is above 45 nm, the substrate and dielectric environment remains constant with the further increase of the thickness of bottom *h*-BN. Hence, the decay of plasmonic interaction becomes the dominating factor. As a result, the PL intensity decreases with the further increase of bottom *h*-BN thickness. To confirm the scenario above, PLs from more positions with different thicknesses were measured as shown in Figure 4b. The thickness dependence clearly shows an optimized thickness of bottom *h*-BN, which is consistent with the result in Figure 4a.

As discussed above, the bottom *h*-BN mainly affects the excitonic properties. We expect that the ratio between trion and exciton increases with the improvement of flatness. The evolution of ratio (trion/exciton) with the change of bottom *h*-BN thickness is shown in Figure 4c. At 293 K, the ratio, dominated by thermal dissociation, is less than 1 and increases slightly with the increase of bottom *h*-BN thickness. At 80 K, the ratio between trion and exciton is more than 1 (thermal dissociation weakened at 80 K), and it increases more significantly compared with that measured at 293 K. Overall, the trion/exciton ratio increases with the increase of bottom *h*-BN thickness. This trend is in sharp contrast to the dependence shown in Figure 4b, which indicates that, besides the global enhancement, the individual intensity enhancement for different excitonic modes is dissimilar because thicker bottom *h*-BN can screen more effectively the long-range Coulomb interaction between WS<sub>2</sub> and silver nano-disk arrays.<sup>[34]</sup> Besides the screening of charge impurities and traps on the surface, thicker *h*-BN also enhances the flatness, which increases the diffusion length of excitons, thus favoring the formation of trions in WS<sub>2</sub>.<sup>[35]</sup> It is worth noting that the traps in the *h*-BN may also contribute to the formation of trion.<sup>[36]</sup> Nevertheless, the full encapsulation isolates the TMDs, ensuring an enclosed environment for the stable optical process.

It is straightforward to prepare the plasmonic arrays directly on top of the TMDs monolayers to fabricate the conventional hybrid TMD-metasurface structures. As a direct comparison with the present flip-over structure, we also fabricated devices with a conventional layout, where metasurface is deposited on top of TMDs with an isolation layer ( $\approx 2$  nm Al<sub>2</sub>O<sub>3</sub>) which prevents the quenching effect between the metasurface and TMDs. The PL measurements in these control samples show that coating an Al<sub>2</sub>O<sub>3</sub> layer directly on WS<sub>2</sub> reduces the PL intensity. And fabricating nano-disk array ( $D = 180$  nm,  $P = 320$  nm) on top of WS<sub>2</sub>/Al<sub>2</sub>O<sub>3</sub> does not show the expected PL enhancement. Instead, the PL intensity decreases after adding the metasurface (Figure S2, Supporting Information). This suggests that, competing with the plasmonic enhancement effect, integrating the metasurface on top of the TMDs not only blocks the free path for the optical excitation and emission, but also modify

the electronic properties of TMDs. The combined contribution is overwhelmed by the blocking and degradation effect that eventually suppresses PL from WS<sub>2</sub>. This direct comparison confirms the advantages of choosing the present flip-over structure.

The strongest enhancement from the surface plasmon is expected by depositing the TMD monolayers directly on top of the metasurface, where the decay of the plasmonic mode is minimized. On the other hand, laminating a flexible monolayer onto the metasurface can form a conforming interface at the room temperature. The tight wrapping onto the metasurface of tens of nanometer thick can also cause large stress in the monolayers. Therefore, without the *h*-BN encapsulation, the WS<sub>2</sub> can easily crack after building up larger stress in a few cooling down/warming up cycles. This breakdown can significantly affect the PL of the WS<sub>2</sub> monolayer because the mechanical detachment can cause the decoupling between WS<sub>2</sub> excitons and plasmonic lattice. Therefore, mechanically, it is also essential to adopt the *h*-BN encapsulation structure. Having *h*-BN encapsulation (especially bottom *h*-BN) can ensure the structural integrity by releasing the strain and deformation caused by the uneven Ag arrays, protecting the WS<sub>2</sub> from the mechanical breakdown (Figure S3, Supporting Information).

Furthermore, using bottom *h*-BN of high dielectric constant can also improve the dielectric environment of both plasmonic arrays and WS<sub>2</sub>. Thus, this can improve the overall PL of the device. Therefore, for a fixed height of the metasurface, the optimal thickness of bottom *h*-BN is correlated to the pitch size. For a typical pitch size,  $P = 260$  nm, the bottom *h*-BN of 6 nm thick performs better than 12 nm (Figure 3). Whereas, when  $P = 320$  nm, the best thickness for the bottom *h*-BN is between 25.5 and 45 nm (Figure 4). These comparisons indicate that the optimal thickness of the bottom *h*-BN depends on the geometry and morphology of the plasmonic arrays. Thicker bottom *h*-BN can improve the substrate flatness and dielectric environment.<sup>[37,38]</sup> And a better dielectric environment promotes the formation of exciton and the transformation from excitons to trions. Nevertheless, a larger thickness also causes the reduction of plasmonic coupling. Since the length scale of plasmonic coupling is in the order of the half the optical wavelength, this gives an ample range for optimizing the thickness of the bottom *h*-BN for the excitonic process in TMDs.

### 3. Conclusion

Both plasmonic array and bottom *h*-BN play the critical roles on PL enhancement in the hybrid structure composed of silver nano-disk arrays and *h*-BN encapsulated WS<sub>2</sub> monolayers. Tuning the geometrical parameters of silver arrays matches the plasmonic resonance with the emission wavelength, adjusting the bottom *h*-BN thickness improves the dielectric environment and substrate flatness, which can effectively enhance the light-matter interactions and the excitonic processes in TMDs both at room temperature and low temperature. By isolating these two effects in different sample geometries, we conclude that the PL enhancement from optimized plasmonic array structures



is the dominating factor that shows stronger enhancement than that contributed from bottom *h*-BN. At 80 and 293 K, we observed  $\approx 13.1$  and  $\approx 15.6$ -fold enhancement from plasmonic coupling ( $P = 320$  nm),  $\approx 8.5$ - and  $\approx 4.4$ -fold PL enhancement from optimized thickness of bottom *h*-BN (thickness = 45 nm), respectively. The flip-over structure, with strong light-matter interaction and structural stability at low temperature, opens up a reliable platform to develop plasmon-enhanced optoelectronic devices, and more paves a way to explore exotic exciton-polariton effects<sup>[39–41]</sup> based on 2D materials and plasmonics.

#### 4. Experimental Section

**Device Fabrication:** The silver nano-disk arrays were fabricated on a cover glass substrate by electron beam lithography. To avoid the oxidation of silver nano-disk and the charge transfer between Ag and WS<sub>2</sub>, around 2 nm Al<sub>2</sub>O<sub>3</sub> was deposited on Ag by ALD at 100 °C. The WS<sub>2</sub> monolayers used in these experiments were grown by molten-salt-assisted CVD<sup>[42]</sup> on 275 nm SiO<sub>2</sub> Si substrate. To pick up the WS<sub>2</sub> easily by polycarbonate film, wafers with WS<sub>2</sub> flakes were soaked in IPA/H<sub>2</sub>O (3:1) solution for 2 h at room temperature. Then the transfer process was proceeding in Argon-filled glove box with the content of both H<sub>2</sub>O and O<sub>2</sub> less than 0.5 ppm.

**Morphology Characterization:** The atomic force microscope (Dimension Icon, Bruker) was used to check the geometry morphology and surface cleanness of *h*-BN. The morphology of nano-disk arrays was characterized by scan electron microscopy (Fei NovaNanoSEM 650).

**Optical Measurements:** The reflection was measured using a white lamp. The reflection is collected within a spot around 10  $\mu$ m. The light is focused and collected by a 100 $\times$  objective with a numerical aperture 0.9. The fluorescence microscopy was excited at 462 nm (objective 100 $\times$ , NA 0.9). The Raman spectrum and PL spectra were measured in an optical cryostat (ST500, Janis) excited at 532 nm (Cobalt Samba 25) using a 100 $\times$  objective with a numerical aperture 0.7. The Raman and PL spectra were resolved by a 500 mm spectrometer (Andor SR-500) and detected by a CCD camera (iDus 420, Andor).

#### Supporting Information

Supporting Information is available from the Wiley Online Library or from the author.

#### Acknowledgements

M.L., P.W., and X.P. acknowledge the funding support from China Scholarship Council (CSC). L.Z. acknowledges support from the Guangdong Province International Postdoctoral Program for Young Talents. The authors thank Jiadong Zhou for the help of CVD growth, thank Heng Zhang and Václav Ocelik for the help of SEM characterization, thank Joost Zoestbergen for technical supports.

#### Conflict of Interest

The authors declare no conflict of interest.

#### Data Availability Statement

Research data are not shared.

#### Keywords

2D materials, hexagonal boron nitride, luminescent devices, plasmon-enhanced photoluminescence, plasmonic structures, WS<sub>2</sub> monolayers

Received: February 24, 2021

Revised: April 22, 2021

Published online: June 19, 2021

- [1] A. F. Koenderink, A. Alu, A. Polman, *Science* **2015**, *348*, 516.
- [2] W. Wang, M. Ramezani, A. I. Väkeväinen, P. Törmä, J. G. Rivas, T. W. Odom, *Mater. Today* **2018**, *21*, 303.
- [3] P. K. Jain, X. Huang, I. H. El-Sayed, M. A. El-Sayed, *Plasmonics* **2007**, *2*, 107.
- [4] G. Lozano, S. R. Rodriguez, M. A. Verschuuren, J. G. Rivas, *Light: Sci. Appl.* **2016**, *5*, e16080.
- [5] Q. Hao, J. Pang, Y. Zhang, J. Wang, L. Ma, O. G. Schmidt, *Adv. Opt. Mater.* **2017**, *6*, 1700984.
- [6] Y. Li, Z. Li, C. Chi, H. Shan, L. Zheng, Z. Fang, *Adv. Sci.* **2017**, *4*, 1600430.
- [7] D. Wang, J. Guan, J. Hu, M. R. Bourgeois, T. W. Odom, *Acc. Chem. Res.* **2019**, *52*, 2997.
- [8] D. Zhang, Y.-C. Wu, M. Yang, X. Liu, C. Ó. Coileáin, M. Abid, M. Abid, J.-J. Wang, I. Shvets, H. Xu, B. S. Chun, H. Liu, H.-C. Wu, *Sci. Rep.* **2016**, *6*, 30320.
- [9] S. Zu, B. Li, Y. Gong, Z. Li, P. M. Ajayan, Z. Fang, *Adv. Opt. Mater.* **2016**, *4*, 1463.
- [10] I. Irfan, S. Golovynskyi, M. Bosi, L. Seravalli, O. A. Yeshchenko, B. Xue, D. Dong, Y. Lin, R. Qiu, B. Li, J. Qu, *J. Phys. Chem. C* **2021**, *125*, 4119.
- [11] K. Zhou, J. Song, L. Lu, Z. Luo, Q. Cheng, *Opt. Express* **2019**, *27*, 2305.
- [12] B. Lee, J. Park, G. H. Han, H.-S. Ee, C. H. Naylor, W. Liu, A. C. Johnson, R. Agarwal, *Nano Lett.* **2015**, *15*, 3646.
- [13] S. Butun, S. Tongay, K. Aydin, *Nano Lett.* **2015**, *15*, 2700.
- [14] Z. Wang, Z. Dong, H. Zhu, L. Jin, M.-H. Chiu, L.-J. Li, Q.-H. Xu, G. Eda, S. A. Maier, A. T. S. Wee, C.-W. Qiu, J. K. W. Yang, *ACS Nano* **2018**, *12*, 1859.
- [15] X. Han, K. Wang, P. D. Persaud, X. Xing, W. Liu, H. Long, F. Li, B. Wang, M. R. Singh, P. Lu, *ACS Photonics* **2020**, *7*, 562.
- [16] D. Wang, M. R. Bourgeois, J. Guan, A. K. Fumani, G. C. Schatz, T. W. Odom, *ACS Photonics* **2020**, *7*, 630.
- [17] W. L. Barnes, A. Dereux, T. W. Ebbesen, *Nature* **2003**, *424*, 824.
- [18] D. Rhodes, S. H. Chae, R. Ribeiro-Palau, J. Hone, *Nat. Mater.* **2019**, *18*, 541.
- [19] B. Auguie, W. L. Barnes, *Phys. Rev. Lett.* **2008**, *101*, 143902.
- [20] P. West, S. Ishii, G. Naik, N. Emani, V. Shalae, A. Boltasseva, *Laser Photonics Rev.* **2010**, *4*, 795.
- [21] W. Liu, B. Lee, C. H. Naylor, H.-S. Ee, J. Park, A. T. C. Johnson, R. Agarwal, *Nano Lett.* **2016**, *16*, 1262.
- [22] S. Rodriguez, M. Schaafsma, A. Berrier, J. G. Rivas, *Phys. B* **2012**, *407*, 4081.
- [23] C. Han, J. Ye, *Nat. Commun.* **2020**, *11*, 713.
- [24] L. Sun, X. Zhang, F. Liu, Y. Shen, X. Fan, S. Zheng, J. T. L. Thong, Z. Liu, S. A. Yang, H. Y. Yang, *Sci. Rep.* **2017**, *7*, 16714.
- [25] H. Zeng, G.-B. Liu, J. Dai, Y. Yan, B. Zhu, R. He, L. Xie, S. Xu, X. Chen, W. Yao, X. Cui, *Sci. Rep.* **2013**, *3*, 1608.
- [26] A. S. Kumbhar, M. K. Kinnan, G. Chumanov, *J. Am. Chem. Soc.* **2005**, *127*, 12444.
- [27] H. Y. Jeong, U. J. Kim, H. Kim, G. H. Han, H. Lee, M. S. Kim, Y. Jin, T. H. Ly, S. Y. Lee, Y.-G. Roh, W.-J. Joo, S. W. Hwang, Y. Park, Y. H. Lee, *ACS Nano* **2016**, *10*, 8192.

- [28] W. Gao, Y. H. Lee, R. Jiang, J. Wang, T. Liu, X. Y. Ling, *Adv. Mater.* **2015**, *28*, 701.
- [29] Z. Wang, Z. Dong, Y. Gu, Y.-H. Chang, L. Zhang, L.-J. Li, W. Zhao, G. Eda, W. Zhang, G. Grinblat, S. A. Maier, J. K. W. Yang, C.-W. Qiu, A. T. S. Wee, *Nat. Commun.* **2016**, *7*, 11283.
- [30] E. M. Purcell, *Biophys. Rev.* **1946**, *69*, 681.
- [31] M. Buscema, G. A. Steele, H. S. J. van der Zant, A. Castellanos-Gomez, *Nano Res.* **2014**, *7*, 561.
- [32] Y. You, X.-X. Zhang, T. C. Berkelbach, M. S. Hybertsen, D. R. Reichman, T. F. Heinz, *Nat. Phys.* **2015**, *11*, 477.
- [33] F. Cadiz, E. Courtade, C. Robert, G. Wang, Y. Shen, H. Cai, T. Taniguchi, K. Watanabe, H. Carrere, D. Lagarde, M. Manca, T. Amand, P. Renucci, S. Tongay, X. Marie, B. Urbaszek, *Phys. Rev. X* **2017**, *7*, 021026.
- [34] Y. Lin, X. Ling, L. Yu, S. Huang, A. L. Hsu, Y.-H. Lee, J. Kong, M. S. Dresselhaus, T. Palacios, *Nano Lett.* **2014**, *14*, 5569.
- [35] J.-W. Kang, J.-W. Jung, T. Lee, J. G. Kim, C.-H. Cho, *Biophys. Rev.* **2019**, *100*, 205304.
- [36] L. Ju, J. Velasco, E. Huang, S. Kahn, C. Nosiola, H.-Z. Tsai, W. Yang, T. Taniguchi, K. Watanabe, Y. Zhang, G. Zhang, M. Crommie, A. Zettl, F. Wang, *Nat. Nanotechnol.* **2014**, *9*, 348.
- [37] L. Wang, Y. Pu, A. K. Soh, Y. Shi, S. Liu, *AIP Adv.* **2016**, *6*, 125126.
- [38] A. Laturia, M. L. V. de Put, W. G. Vandenberghe, *npj 2D Mater. Appl.* **2018**, *2*, 6.
- [39] J. Kasprzak, M. Richard, S. Kundermann, A. Baas, P. Jeambrun, J. M. J. Keeling, F. M. Marchetti, M. H. Szymańska, R. André, J. L. Staehli, V. Savona, P. B. Littlewood, B. Deveaud, L. S. Dang, *Nature* **2006**, *443*, 409.
- [40] A. Amo, J. Lefrère, S. Pigeon, C. Adrados, C. Ciuti, I. Carusotto, R. Houdré, E. Giacobino, A. Bramati, *Nat. Phys.* **2009**, *5*, 805.
- [41] H. Deng, H. Haug, Y. Yamamoto, *Rev. Mod. Phys.* **2010**, *82*, 1489.
- [42] J. Zhou, J. Lin, X. Huang, Y. Zhou, Y. Chen, J. Xia, H. Wang, Y. Xie, H. Yu, J. Lei, D. Wu, F. Liu, Q. Fu, Q. Zeng, C.-H. Hsu, C. Yang, L. Lu, T. Yu, Z. Shen, H. Lin, B. I. Yakobson, Q. Liu, K. Suenaga, G. Liu, Z. Liu, *Nature* **2018**, *556*, 355.